Dependence of Convective Dynamo Action on Bulk Electrical Conductivity

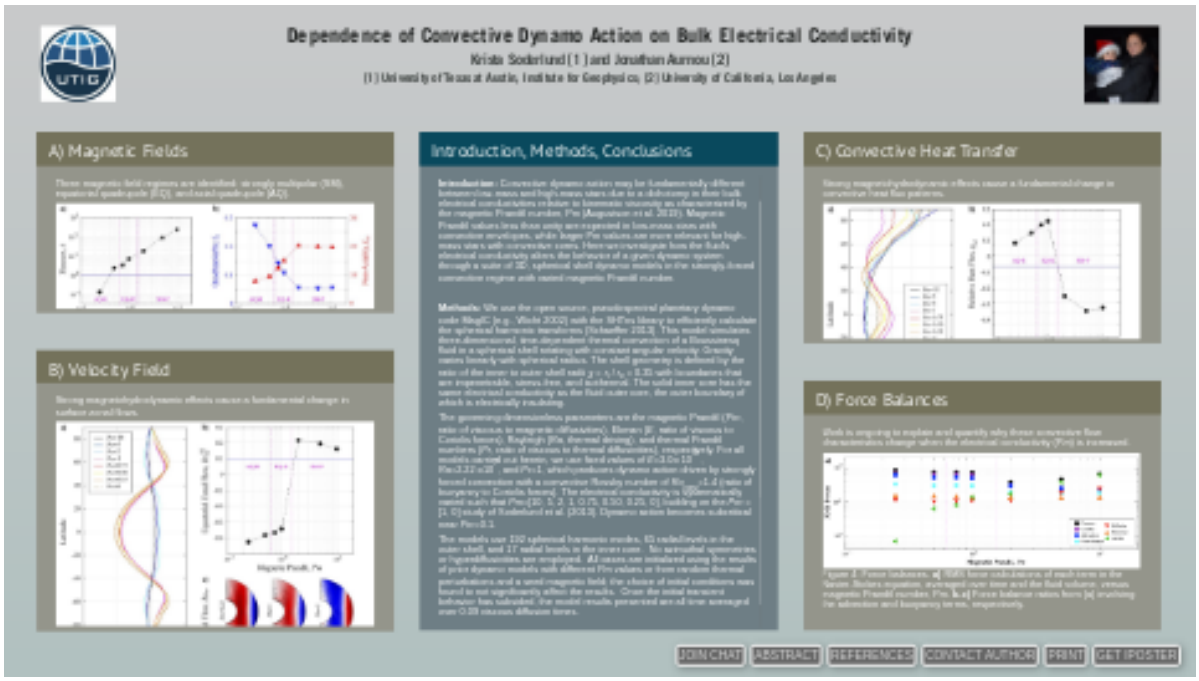

Krista Soderlund [1] and Jonathan Aurnou [2]

[1] University of Texas at Austin, Institute for Geophysics; [2] University of California, Los Angeles

PRESENTED AT:

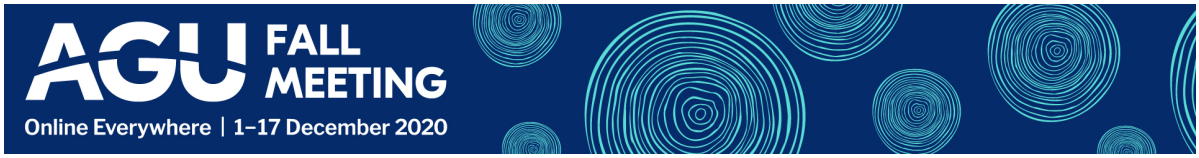

A) MAGNETIC FIELDS

Three magnetic field regimes are identified: strongly multipolar (SM), equatorial quadrupole (EQ), and axial quadrupole (AQ).

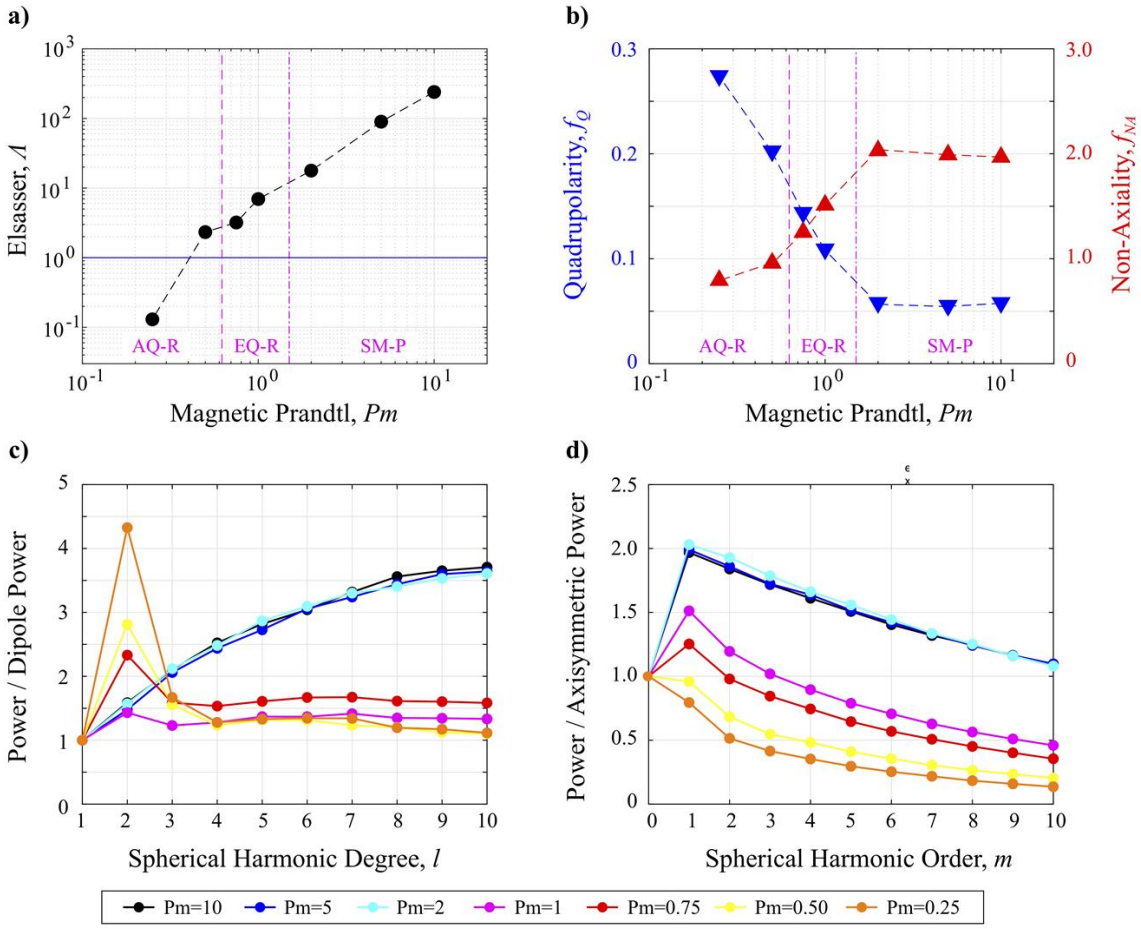

Figure 1: Magnetic field characteristics. **a)** Magnetic field strength as measured by the Elsasser number, Λ, versus the magnetic Prandtl number, *Pm*. **b)** Magnetic field morphology as measured by quadrupolarity, f_Q, and non-axiality, f_{NA}, versus the magnetic Prandtl number, *Pm*. Vertical magenta lines demarcate approximate regime boundaries. **c)** Magnetic power spectra as a function of spherical harmonic degree *l*, normalized by the *l*=1 dipole power. **d)** Magnetic power spectra as a function of spherical harmonic order *m*, normalized by the *m*=0 axisymmetric power. Color denotes *Pm*.

Field Strength:

Dimensionless magnetic field strength is measured by the Elsasser number Λ and relates to the magnetic energy density in the outer core:

$$\Lambda = \frac{\sigma B^2}{\rho\Omega} = 2\mathcal{E}_M PmE \quad \text{where} \quad \mathcal{E}_M = \frac{1}{2V_s}\int \mathbf{B}\cdot\mathbf{B}\, dV.$$

Across the suite of models, the magnetic field strength varies by more than three orders of magnitude increasing from $\Lambda \sim 10^{-1}$ for *Pm*=0.25 to $\Lambda \sim 10^{2}$ for *Pm*=10 in a nearly monotonic trend (Fig. 1a).

Field Morphology:

Magnetic field morphology is summarized in Figure 1b based on the behavior of the magnetic power spectra of the outer core up to spherical harmonic degree (l) and order (m) 10 shown in panels c and d. The spectra demonstrate that models with $Pm \geq 2$ are characterized by strongly multipolar dynamos with significant power over a broad range of spherical harmonic degrees and a peak in the equatorially symmetric m=1 mode. Conversely, models with $Pm \leq 0.5$ are characterized by a substantial quadrupole (l=2) component that has peak power in the axisymmetric m=0 mode. Intermediate Pm=[0.75, 1.0] models have flatter spectra with some quadrupolar enhancement and preferential equatorial symmetry.

These behaviors are quantified through dipolarity (f_D), quadrupolarity (f_Q), and non-axiality (f_{NA}) parameters:

$$f_D = \frac{\mathcal{P}(l=1)}{\Sigma_{l=1}^{l=10}\mathcal{P}(l)}, \quad f_Q = \frac{\mathcal{P}(l=2)}{\Sigma_{l=1}^{l=10}\mathcal{P}(l)}, \quad f_{NA} = \frac{\mathcal{P}(m=1)}{\mathcal{P}(m=0)}$$

where P is magnetic power at the specified l and m values. Dipolarity does not strongly vary across the survey, but the magnetic field becomes increasingly quadrupolar (larger f_Q) and axisymmetric (smaller f_{NA}) for $Pm \leq 1$. As a result, we define three magnetic field regimes: the strongly multipolar (SM) regime with $f_Q < 0.1$ and $f_{NA} > 1$ values, the equatorial quadrupole (EQ) regime with $f_Q > 0.1$ and $f_{NA} > 1$ values, and the axial quadrupole (AQ) regime with $f_Q > 0.1$ and $f_{NA} < 1$.

B) VELOCITY FIELD

Strong magnetohydrodynamic effects cause a fundamental change in surface zonal flows.

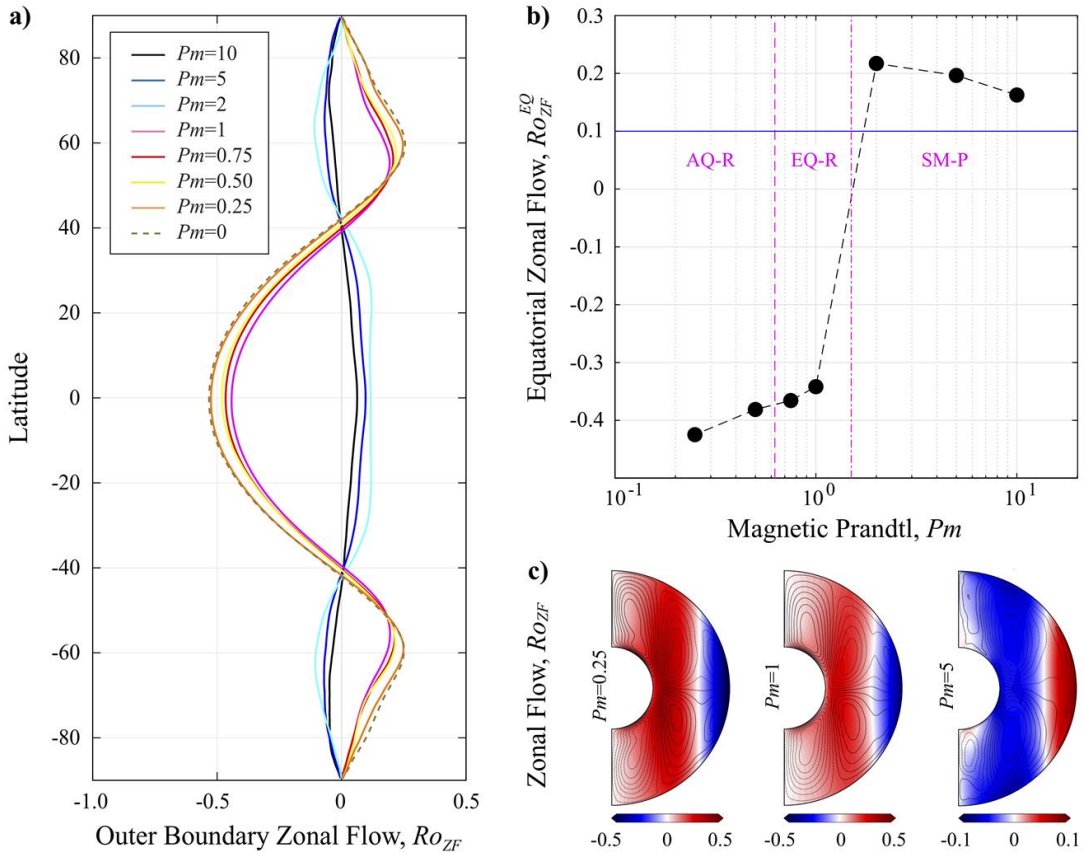

Figure 2: Zonal flow characteristics. **a)** Zonal flow profiles on the outer shell boundary as a function of latitude. Color denotes *Pm*. **b)** Equatorial zonal flow speed from **(a)** versus the magnetic Prandtl number. Vertical magenta lines demarcate approximate regime boundaries. **c)** Zonal flows and meridional circulations for the (left) *Pm*=0.25, (middle) *Pm*=1, and (right) *Pm*=5 cases, averaged over time and longitude. In all panels, flow speeds are given in Rossby number units, $Ro_{ZF}=U_\Phi/\Omega D$, and red (blue) indicates the prograde (retrograde) flow direction. Solid (dashed) black contours denote clockwise (counterclockwise) circulations.

Flow Speeds:

Dimensionless flow speeds are measured by the Rossby number *Ro* and relate to the kinetic energy density through

$$Ro = \frac{U}{\Omega D} = \sqrt{2\mathcal{E}_K}E \quad \text{where} \quad \mathcal{E}_K = \frac{1}{2V_s}\int \mathbf{u}\cdot\mathbf{u}\, dV.$$

In order to show the relative contributions of non-axisymmetric convective contributions, we also calculate the non-axisymmetric Rossby number $Ro_{na}=U_{na}/\Omega D$, where U_{na} is the rms flow speed excluding the axisymmetric components. Strong magnetic fields act to reduce the global flow speeds by nearly a factor of two in the $Pm \geq 2$ models compared to those with $Pm \leq 1$ and further promote the relative non-axisymmetric convective component by damping the zonal flows more strongly.

Zonal Flows:

A fundamental change in zonal flow also occurs in our survey. Figure 2a shows the time-averaged zonal winds on the outer shell boundary as a function of latitude. Two distinct styles of zonal flow are found. A strong retrograde equatorial jet and flanking prograde jets form when $Pm \leq 1$. Zonal flows in models with $Pm \geq 2$ are fundamentally different where, instead, a broad

prograde equatorial jet dominates with retrograde flow near and interior to the tangent cylinder. Further, the wind speeds in the prograde jet regime are only about half that of those in the retrograde jet regime. Figure 2b, which shows the zonal velocity on the outer boundary at the equator as a function of *Pm*, further quantifies this behavior and demonstrates that increasing the electrical conductivity (*Pm*) can cause the direction of zonal jets to reverse. As a result, we further define the dynamical regimes as SM-P, EQ-R, AQ-R to denote whether the equatorial jets are prograde (P) or retrograde (R).

Although the meridional circulations have similar trends in all of our models, important differences are evident (Fig. 2c). Each hemisphere develops two large circulation cells with opposite polarities within and outside of the tangent cylinder and across the equator. The circulation patterns differ, however, at large cylindrical radii. While smaller cells near the outer shell boundary occur in both regimes, their polarities are reversed. The cells reinforce the large-scale circulation pattern outside the tangent cylinder in the $Pm \leq$ models, but oppose it in the $Pm \geq 2$ models. This difference is likely important for the generation of zonal flows described above and the pattern of convective heat transfer described below.

INTRODUCTION, METHODS, CONCLUSIONS

Introduction: Convective dynamo action may be fundamentally different between low-mass and high-mass stars due to a dichotomy in their bulk electrical conductivities relative to kinematic viscosity as characterized by the magnetic Prandtl number, Pm (Augustson et al. 2019). Magnetic Prandtl values less than unity are expected in low-mass stars with convective envelopes, while larger Pm values are more relevant for high-mass stars with convective cores. Here we investigate how the fluid's electrical conductivity alters the behavior of a given dynamo system through a suite of 3D, spherical shell dynamo models in the strongly-forced convective regime with varied magnetic Prandtl number.

Methods: We use the open source, pseudospectral planetary dynamo code MagIC (e.g., Wicht 2002) with the SHTns library to efficiently calculate the spherical harmonic transforms (Schaeffer 2013). This model simulates three-dimensional, time-dependent thermal convection of a Boussinesq fluid in a spherical shell rotating with constant angular velocity. Gravity varies linearly with spherical radius. The shell geometry is defined by the ratio of the inner to outer shell radii $\chi = r_i / r_o = 0.35$ with boundaries that are impenetrable, stress-free, and isothermal. The solid inner core has the same electrical conductivity as the fluid outer core, the outer boundary of which is electrically insulating.

The governing dimensionless parameters are the magnetic Prandtl (*Pm*, ratio of viscous to magnetic diffusivities), Ekman (*E*, ratio of viscous to Coriolis forces), Rayleigh (*Ra*, thermal driving), and thermal Prandtl numbers (*Pr*, ratio of viscous to thermal diffusivities), respectively. For all models carried out herein, we use fixed values of $E=3.0\times10^{-4}$, $Ra=2.22\times10^{7}$, and $Pr=1$, which produces dynamo action driven by strongly forced convection with a convective Rossby number of $Ro_{conv}=1.4$ (ratio of buoyancy to Coriolis forces). The electrical conductivity is systematically varied such that *Pm*=[10, 5, 2, 1, 0.75, 0.50, 0.25, 0], building on the *Pm* = [1, 0] study of Soderlund et al. (2013). Dynamo action becomes subcritical near *Pm*=0.1.

The models use 192 spherical harmonic modes, 65 radial levels in the outer shell, and 17 radial levels in the inner core. No azimuthal symmetries or hyperdiffusivities are employed. All cases are initialized using the results of prior dynamo models with different *Pm* values or from random thermal perturbations and a seed magnetic field; the choice of initial conditions was found to not significantly affect the results. Once the initial transient behavior has subsided, the model results presented are all time averaged over 0.09 viscous diffusion times.

Conclusions: Our results show that the fluid motions, the pattern of convective heat transfer, and the mode of dynamo generation all differ across the range $0.25 \leq \mathrm{Pm} \leq 10$ as shown in the surrounding four panels. Thus, our work further supports the importance of bulk electrical conductivity for not only sustaining dynamo action, but also for the characteristics of the large-scale convective flows that generate those dynamo fields.

Acknowledgments: This work was supported by NASA Grant NNX15AL56G with computational resources provided by the NASA High-End Computing (HEC) Program through the NASA Advanced Supercomputing (NAS) Division at Ames Research Center. The MagIC code is publicly available at https://magic-sph.github.io/contents.html.

C) CONVECTIVE HEAT TRANSFER

Strong magnetohydrodynamic effects cause a fundamental change in convective heat flux patterns.

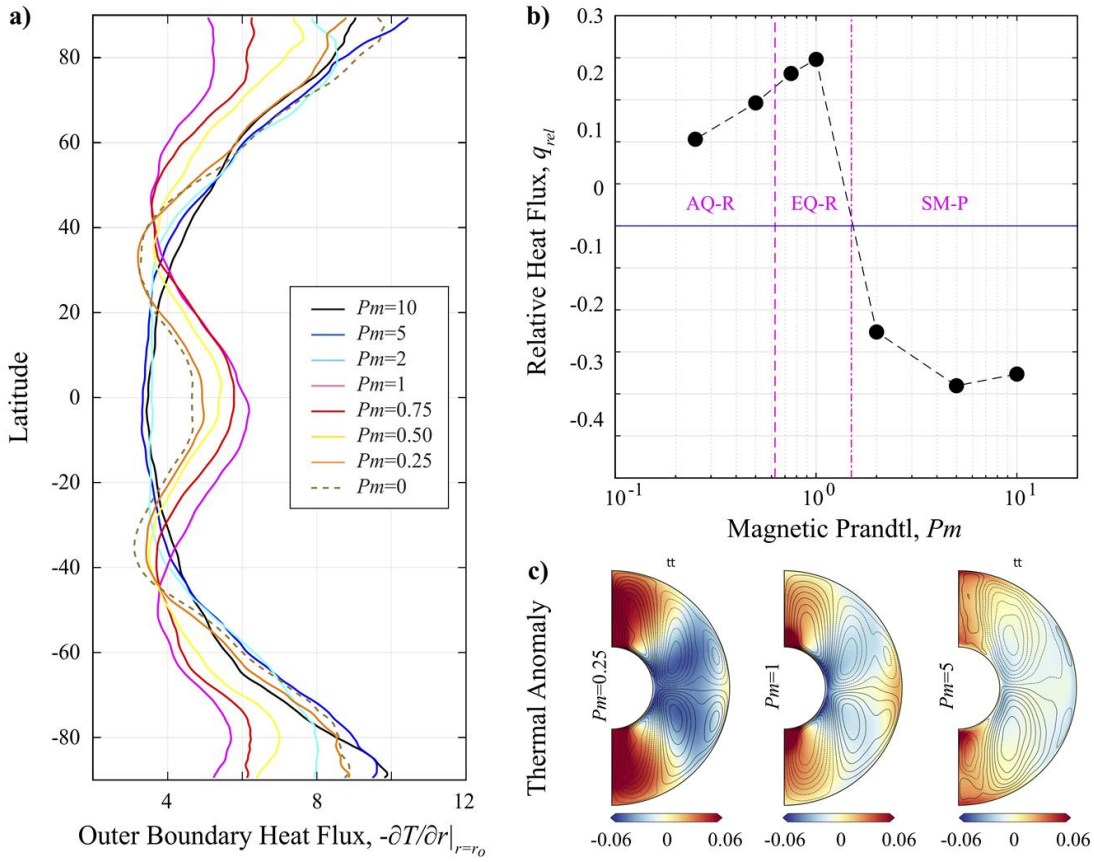

Figure 3: Convective heat transfer characteristics. **a)** Dimensionless heat flux on the outer shell boundary as a function of latitude. Color denotes *Pm*. **b)** Relative heat flux between the equator and mid-latitudes from **(a)** versus the magnetic Prandtl number. Vertical magenta lines demarcate approximate regime boundaries. **c)** Dimensionless thermal anomalies for the (left) *Pm*=0.25, (middle) *Pm*=1, and (right) *Pm*=5 cases; superimposed solid (dashed) black contours denote clockwise (counterclockwise) circulations.

Efficiency:

Heat transfer efficiency is measured by the Nusselt number, or the ratio of total to conductive heat flux:

$$Nu = \frac{r_o}{r_i}\frac{qD}{\rho C_p \kappa \Delta T}$$

The Nusselt number ranges from *Nu* = 12.6 in the SM-P regime to *Nu* = 13.5 in the EQ-R regime. Comparing against the non-magnetic value of *Nu* = 13.0, the dynamo can therefore act to both diminish and enhance convective heat transfer depending on the magnetic Prandtl number.

Convective Heat Flux Patterns:

Similar to the zonal flows, two distinct styles of heat transfer profiles are found across our survey. Figure 3a compares the outer boundary heat fluxes as a function of latitude. For models in the SM-P regime with $Pm \geq 2$, heat transfer varies smoothly latitude from a minimum at the equator to peaks at the poles. Conversely, for models in the EQ-R and AQ-R regimes, a secondary peak develops at low latitudes. This peak is similar in amplitude to the poles in the *Pm*=1 model and becomes less prominent as Pm is decreased. Figure 3b further quantifies this behavior through a relative heat flux parameter, q_{rel}:

$$q_{rel} = \frac{(q_{EQ} - \overline{q_{45^o N}^{45^o S}})}{q_{EQ}},$$

The change in sign across the EQ-R -- SM-P regime transition demonstrates that increasing the electrical conductivity (*Pm*) can also drive significant changes in the spatial distribution of convective heat transfer.

Figure 3c shows the thermal anomalies for models in each behavioral regime. All models have enhanced temperatures near the poles because strong upwellings develop here, regardless of the magnetic Prandtl number, indicating that meridional circulations largely control the heat transfer. The equatorial peaks in the *Pm* =[0.25, 1] models also correspond to regions of radially outward flow enhancement. In contrast, heat flux is minimal near the equator in the *Pm*=5 model because upwelling flows are locally weak here.

D) FORCE BALANCES

Work is ongoing to explain and quantify why these convective flow characteristics change when the electrical conductivity (*Pm*) is increased.

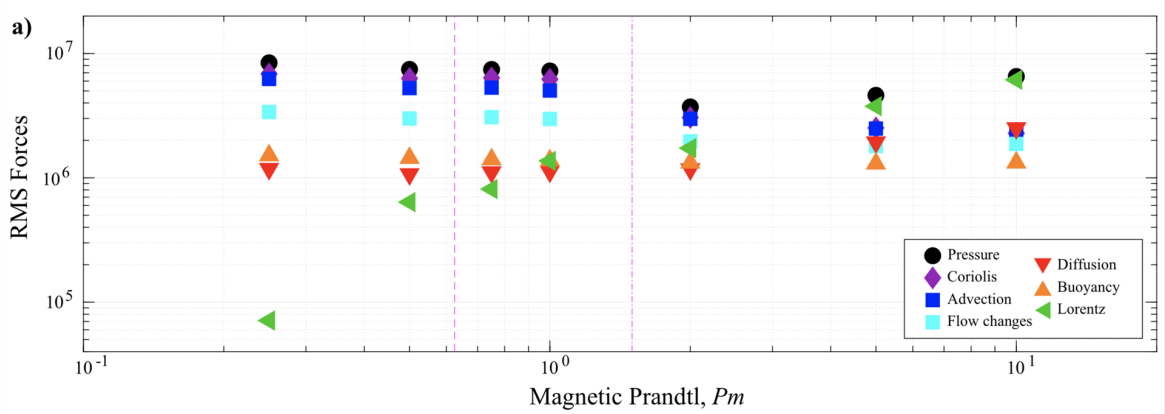

Figure 4: Force balances. **a)** RMS force calculations of each term in the Navier-Stokes equation, averaged over time and the fluid volume, versus magnetic Prandtl number, *Pm*. **b-c)** Force balance ratios from (a) involving the advection and buoyancy terms, respectively.

Figure 4 shows the room mean square (RMS) forces in our models to illustrate how the force balance evolves across the survey. At low magnetic Prandtl numbers in the AQ-R and EQ-R regimes, the primary force balance is between the pressure gradient, Coriolis, and Advection terms of the Navier-Stokes equation with smaller contributions due to flow changes, buoyancy, diffusion, and Lorentz forces (Fig. 4a). At the other extreme with large *Pm* values, the dominant force balance in the SM-P regime is between the pressure gradient and Lorentz forces with buoyancy becoming the smallest contributor.

With no clear change in global force balance across the AQ-R and EQ-R regime boundary, we will next consider spectral calculations of RMS forces (Aubert et al. 2017; Schwaiger et al. 2019) to further investigate why these dynamical changes occur across our survey.

ABSTRACT

Convective dynamo action may be fundamentally different between low-mass and high-mass stars due to a dichotomy in their bulk electrical conductivities relative to kinematic viscosity as characterized by the magnetic Prandtl number, *Pm* (Augustson et al., 2019, https://doi.org/10.3847/1538-4357/ab14ea (https://doi.org/10.3847/1538-4357/ab14ea)). Magnetic Prandtl values less than unity are expected in low-mass stars with convective envelopes, while larger Pm values are more relevant for high-mass stars with convective cores. Here we investigate how the fluid's electrical conductivity alters the behavior of a given dynamo system through a suite of 3D, spherical shell dynamo models in the strongly-forced convective regime with varied magnetic Prandtl number. We find that the fluid motions, the pattern of convective heat transfer, and the mode of dynamo generation all differ across the range $0.25 \leq Pm \leq 10$. For example, we show that strong magnetohydrodynamics effects cause a fundamental change in the surface zonal flows: the equatorial zonal jet reverses direction for sufficiently large values of the electrical conductivity. Thus, our work further supports the importance of bulk electrical conductivity for not only sustaining dynamo action, but also for the characteristics of the large-scale convective flows that generate those dynamo fields.

REFERENCES

Aubert, J., Gastine, T., & Fournier, A. (2017). Spherical convective dynamos in the rapidly rotating asymptotic regime. Journal of Fluid Mechanics, 813, 558-593.

Augustson, K. C., Brun, A. S., & Toomre, J. (2019). Rossby and magnetic Prandtl number scaling of stellar dynamos. The Astrophysical Journal, 876(1), 83.

Soderlund, K. M., Heimpel, M. H., King, E. M., & Aurnou, J. M. (2013). Turbulent models of ice giant internal dynamics: Dynamos, heat transfer, and zonal flows. Icarus, 224(1), 97-113.

Schwaiger, T., Gastine, T., & Aubert, J. (2019). Force balance in numerical geodynamo simulations: a systematic study. Geophysical Journal International, 219, S101-S114.

Wicht, J. (2002). Inner-core conductivity in numerical dynamo simulations. Physics of the Earth and Planetary Interiors, 132(4), 281-302.